



Article

# Highly Efficient Nanostructured Bi<sub>2</sub>WO<sub>6</sub> Thin Film Electrodes for Photoelectrochemical and Environment Remediation

Bandar Y. Alfaifi <sup>1</sup>, Hossein Bayahia <sup>2</sup> and Asif Ali. Tahir <sup>1,\*</sup>

<sup>1</sup> Environment and Sustainability Institute (ESI), University of Exeter, Penryn Campus, Penryn, Cornwall TR10 9FE, UK; ba283@exeter.ac.uk

<sup>2</sup> Chemistry Department, Faculty of Science, Albaha University, Albaha 65527, Saudi Arabia; hbayahia@bu.edu.sa

\* Correspondence: a.tahir@exeter.ac.uk

Received: 16 April 2019; Accepted: 10 May 2019; Published: 17 May 2019



**Abstract:** Nanostructured Bi<sub>2</sub>WO<sub>6</sub> thin film electrodes with enhanced solar energy conversion and photocatalytic properties have been fabricated using Aerosol-Assisted Chemical Vapor Deposition (AACVD). By conveniently controlling the deposition process parameters, Bi<sub>2</sub>WO<sub>6</sub> electrodes were fabricated with nanoplates and hierarchical buckyball-shaped microsphere structures morphology. A detailed study has been conducted to correlate the structure and morphology with the photoelectrochemical (PEC) and photocatalytic dye degradation performance. The PEC investigations revealed that the hierarchical buckyball-shaped microsphere structured Bi<sub>2</sub>WO<sub>6</sub> electrodes have shown the photocurrent density of 220  $\mu\text{Acm}^{-2}$  while nanoplates have a photocurrent density of 170  $\mu\text{Acm}^{-2}$  at 0.23 V (vs. Ag/AgCl/3M KCl) under AM1.5 illumination. The PEC characterization of Bi<sub>2</sub>WO<sub>6</sub> electrodes also reveals that the photocurrent density and photocurrent onset potential is strongly dependent on the orientation and morphology, hence the deposition parameters. Similarly, the methylene blue (MB) and rhodamine B (RhB) photodegradation performance of Bi<sub>2</sub>WO<sub>6</sub> electrodes also show a strong correlation with morphology. This finding provides an appropriate route to engineer the energetic and interfacial properties of Bi<sub>2</sub>WO<sub>6</sub> electrode to enhance solar energy conversion and the photocatalytic performance of semiconductor materials.

**Keywords:** Bi<sub>2</sub>WO<sub>6</sub>; nanostructures; microsphere structures; thin films; photoelectrochemical; photocatalyst; methylene blue; rhodamine B

## 1. Introduction

The fabrication of nanostructured materials with well-defined shapes and morphology has been considered a great challenge in material chemistry and nanotechnology [1,2]. In recent times, the strong relationship between morphology and performance has been acknowledged as an important factor to be aware of while designing the profile and organization of nanomaterials [3,4]. Nanomaterials with well-designed surface features have been inspiring significant research due to their vital functions in the study of structure-property interactions [5,6]. Well-organized hierarchical morphologies of inorganic compounds offer innovative chemical, as well as physical, properties because the benefits of materials lie in the nature of their microstructure as well as their nanostructure [7]. The conventional procedures for scheming the morphology (structural arrangement and size) of nanomaterials are mainly dependent on two basic approaches: first is the chemical approach which includes the hydrothermal process [8], surfactant templating [9], as well as molecular assembly [10] and so on; the second is the physical strategy, mainly based on thermal evaporation [11] and physical exfoliation [12].

Despite the successful preparation of monodispersed spherical particles, one-dimensional nanorods and nanowires, the deposition of nanoelectrodes possessing the desired characteristics remains difficult. Several deposition procedures—viz. pulsed laser deposition [13], reactive sputtering [14], spin-coating [15], spray pyrolysis [16] sol-gel [17,18] and chemical vapor deposition [19]—have already been applied for the deposition of thin film electrodes with controlled shape and morphology.

Among the aforementioned electrode deposition methods, the aerosol-assisted chemical vapor deposition (AACVD) is facile, possesses advantages such as solo solution and may be applied to the preparation of multicomponent electrodes. Significant efforts have been made to prepare  $\text{Bi}_2\text{WO}_6$  particles by hydrothermal process and then the deposition of thin film electrodes using the dip-coating method [20], spin coating [21], spray pyrolysis [22] and an electrostatic layer by layer deposition procedure [23]. However, to the best of author's knowledge, some information is available in the literature regarding the deposition of  $\text{Bi}_2\text{WO}_6$  electrodes using AACVD. Ishikawa et al. prepared  $\text{Bi}_2\text{WO}_6$  thin films by metal organic chemical vapor deposition (MOCVD) utilizing a vertical cold-wall reactor. Trimethyl bismuth and pentaethoxy tungsten have been applied as the Bi and W precursors in the presence of  $\text{O}_2$  gas as an oxidant [19].

$\text{Bi}_2\text{WO}_6$  has received noteworthy consideration owing to its successful use both as a photocatalyst [24] and a semiconductor material in photoelectrochemical (PEC) water splitting [25–29] as well as in  $\text{CO}_2$  reduction [30]. It has been reported that the photocatalytic activity and PEC characteristics of  $\text{Bi}_2\text{WO}_6$  nanomaterials closely correlate with their particle dimensions and surface features, as well as their structural organization.

In most photocatalytic processes, a suspended powder is used as a photocatalyst with reduced photocatalytic activity. A difficult recollection process is a major barrier to realizing a large scale application of photocatalysis [31]. Nanostructured thin film electrode has the potential to overcome this barrier and nanostructured electrodes possess many advantages such as a high internal surface aspect ratio, excellent porosity and tremendous photocatalytic activity [31]. However, the problem of synthesizing cost-effective crystalline nanofilm electrodes of  $\text{Bi}_2\text{WO}_6$  on a transparent substrate has not yet been fully resolved.

In this work,  $\text{Bi}_2\text{WO}_6$  nanostructured electrodes with different morphologies were fabricated by Aerosol Assisted Chemical Vapor Deposition (AACVD). The cost-effective and facile AACVD approach is reproducible. We have fabricated  $\text{Bi}_2\text{WO}_6$  nanostructured electrodes that have diverse morphologies, for instance nanoplates and hierarchical buckyball-shaped microsphere structures, by expediently controlling the process factors of AACVD. Moreover, the electrodes prepared in this work have shown remarkable photoelectrochemical activity and efficient photocatalytic degradation of methylene blue (MB) and rhodamine B (RhB) dyes. Our research will certainly contribute considerably to the future development of  $\text{Bi}_2\text{WO}_6$  as a prospective semiconductor material for related such as electrochemical energy storage, photocatalysis, self-cleaning, sensors, photo-responsive switches, thermoelectric devices and electro-ceramics. The preparation method described here has the ability to expand the morphology controlled fabrication of related materials.

## 2. Experimental

### 2.1. Materials

Fluorine-doped tin oxide (FTO) coated glass (TEC 8 Pilkington,  $8 \Omega/\text{square}$ ) were employed as the substrate and were cleaned by sonication in acetone, ethanol and distilled water for 10 min each and stored in ethanol until later use. All other analytical grade chemicals and reagents were purchased from Sigma-Aldrich (UK) and used without further purification. Distilled water was used throughout the experiment.

## 2.2. Preparation of Precursor Solution

0.9 g of  $\text{Bi}_2\text{O}_3$  powder and 0.5 g of  $(\text{NH}_4)_6\text{H}_2\text{W}_{12}\text{O}_{40}\cdot\text{XH}_2\text{O}$  powder were added to a mixture of 10 mL of acetic acid and 5 mL of dimethylaminopropanol (DMAP). The above suspension was stirred and heated to 100 °C until the mixture became a transparent solution. Once the above solution became clear and after cooling to room temperature, the mixture was diluted to 100 mL by adding dimethylformamide to make the precursor solution.

## 2.3. Fabrication of Electrodes by AACVD

In a typical deposition, 15 mL precursor solution was taken in a 50 mL round-bottom flask and placed above the piezoelectric modulator of an ultrasonic humidifier. Air at a flow rate of 300 mL/min was used as the carrier gas and the flow rate was controlled by a L1X linear flowmeter. The generated aerosol droplets of the precursor were transferred to the heated reactor by the carrier gas [32]. The substrate was placed in the reactor (hotplate surface) so that aerosol reaches the Fluorine doped tin oxide (FTO) glass substrate and falls vertically from the top. The substrate was heated up to the deposition temperature for 20 min before the deposition starts. The deposition experiments were repeated several times to verify the reproducibility and controllability of the process. Controlled experiments were also carried out using an aqueous solution of  $\text{Bi}(\text{NO}_3)_3\cdot 5\text{H}_2\text{O}$  and  $(\text{NH}_4)_6\text{H}_2\text{W}_{12}\text{O}_{40}\cdot\text{XH}_2\text{O}$ .

## 2.4. Material Characterization

The material phase composition was determined using a Bruker D8 Advance X-ray diffractometer (XRD, Billerica, MA, USA) (Cu  $\text{K}\alpha$  irradiation, 40 kV/40 mA,  $0.02^\circ$   $2\theta$  step size and a scan time of 3 s per step) in the range of  $20$ – $70^\circ$   $2\theta$ . The morphology and composition of the thin film were characterized using a high-resolution scanning electron microscope (HITACHI S3200N SEM, Tokyo, Japan) coupled with energy dispersive spectroscopy (EDS; Oxford instrument elemental analysis). Raman spectroscopy was undertaken using a HORIBA Jobin Yvon LabRAM HR Raman Spectrophotometer, Kyoto, Japan (with 632.8 nm He-Ne laser). The spectrum was recorded in the range of 100 to 1600  $\text{cm}^{-1}$ .

Absorption spectra were measured on a lambda 1050 with 150 mm integrated InGaAs sphere Perkin-Elmer UV-Vis spectrophotometer in the wavelength range of 200–800 nm.

## 2.5. Photoelectrochemical and Photocatalytic Characterisation

The photoelectrochemical (PEC) efficiency of  $\text{Bi}_2\text{WO}_6$  photoelectrodes was determined in 1 M NaOH solution (pH = 13), with the help of 300 W xenon lamp coupled with an AM 1.5 filter (Newport 66902). An electrochemical cell with three probes has been employed in the electrochemical observation. Linear sweep voltameter was employed for photocurrent calculation in +0.35 to  $-0.35$  V range. Photodegradation of methylene blue (MB) and rhodamine B (RhB) was in 60 mL of a 10 mg/L solution using 1 mL of  $\text{H}_2\text{O}_2$  as a catalyst. The degradation efficiency ( $C/C_0$ ), was calculated by measuring the dye absorption at wavelengths 653 nm and 554 nm for MB and RhB, respectively. Herein, the  $C_0$  indicates the initial concentration of the dye whereas C is the concentration at different time intervals.

## 3. Result and Discussion

In the present study, the synthesis of  $\text{Bi}_2\text{WO}_6$  nanoelectrodes was accomplished using the one-step approach, utilizing AACVD procedures. As described in the experimental section of this manuscript, the impact of deposition temperature and carrier gas flow on the structure and photocatalytic activity of the electrodes was studied. Briefly, the electrodes deposition showed better performance compared to that in the existing literature, owing to one-step fabrication and deposition. The electrode showed fine adhesion and excellent stability during the photocatalytic experiments.

### 3.1. Material Characterization

The XRD spectra of the deposited electrodes correspond to the orthorhombic phase (Russellite)  $\text{Bi}_2\text{WO}_6$  with space group B2ab (Figure 1), in addition to the peaks indexed as Fluorinated  $\text{SnO}_2$  layer used as substrate. The obtained XRD spectra are consistent with previous spectra present in the literature for  $\text{Bi}_2\text{WO}_6$  (ICDD 01-073-2020) [33].

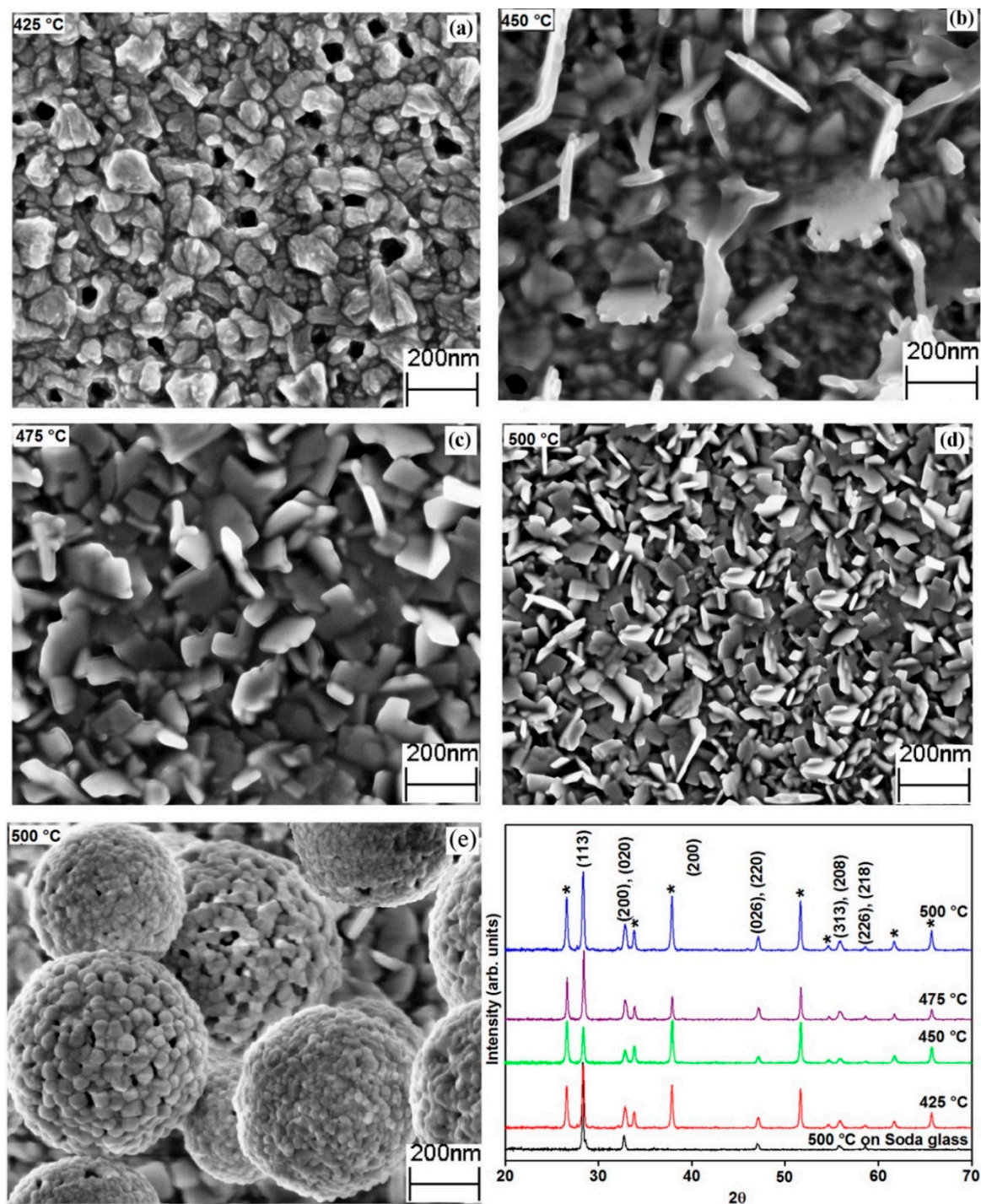


**Figure 1.** The scanning electron microscope (SEM) images (a–d) deposited at 300mL/min flow rate (e) at 500 °C with 100 mL/min carrier gas flow. The X-ray diffraction (XRD) spectra of electrodes at deposition temperature of 425–500 °C, the peaks marked with (\*) belong  $\text{SnO}_2$  arises from the Fluorine doped tin oxide (FTO) substrate.

The Raman spectroscopic data of  $\text{Bi}_2\text{WO}_6$  electrodes is illustrated in Figure S1 (supporting information) and the peaks at 760 and 790  $\text{cm}^{-1}$  were indexed to the asymmetric and symmetric  $A_g$  modes of terminal O–W–O chain in  $\text{Bi}_2\text{WO}_6$  [34]. The peak at 310  $\text{cm}^{-1}$  was assigned to  $\text{Bi}^{3+}$  and  $\text{WO}_4$  whereas the terminal  $\text{WO}_2$  group was assigned to peaks at 300  $\text{cm}^{-1}$ . The peaks in the wavelength range of 700–1000  $\text{cm}^{-1}$  were assigned to W–O bonds [35].

### 3.2. Deposition Temperature Effect on Morphology and Crystallinity

The impact of deposition condition on the morphology of  $\text{Bi}_2\text{WO}_6$  electrodes was carried out extensively in the present study. Different substrate temperatures were applied to find out the effect on the crystallinity and morphology, however; the rest of the variables remained the same.

To investigate the deposition temperature effect on structure and morphology, at various temperatures, electrodes were deposited by using AACVD. Figure 1 depicts the XRD patterns of  $\text{Bi}_2\text{WO}_6$  electrodes at various deposited temperatures with their respective morphology and structure. The XRD peaks were prominent and intensify gradually, indicating better crystallinity with increasing temperatures (425–500 °C). The unidentified peaks present in the spectra of XRD (Figure 1) of the electrode deposited at 425 °C disappeared with the rise in temperature, signifying that these peaks may correspond to un-decomposed materials. The crystallite size calculated on the basis of peak expansion (113) using the Scherrer equation is about 41 nm. The SEM micrograph of the electrode (Figure 1a) indicates a dense homogeneously dispersed microstructure without any distinguishable features. As shown in Figure 1b, nanoplates started to emerge from the dense microstructures, as the temperature of the deposition increased to 450 °C. Figure 1b illustrates that the size and form of the nanoplates are not well defined although long edges were clearly visible. As the temperature of deposition was further amplified to 475 °C, the electrode structure depicted specific plate-like morphology possessing narrow edges. An additional increase in temperature of deposition to 500 °C resulted in big and thin nanoplates. The length of the edge of an average nanoplate is about 110 nm, with a width of about 10 nm. Figure 1d demonstrates that the nanoplates that emerged from the substrate were aligned perpendicular to the FTO base.

### 3.3. Effect of Carrier Gas on Morphology

Although the carrier gas flow can potentially influence the deposition temperature due to the cooling effect, the change of carrier gas flow had no pronounced effect on the morphology of electrodes deposited below 500 °C. Surprisingly, the amplification of the temperature of the deposition to 500 °C and simultaneous reduction of the carrier gas flow rate to 100 mL/min resulted in the formation of hierarchical buckyball-shaped microsphere structured electrodes (Figure 1e). Further SEM analysis (Figure 2a,c) showed that the buckyball-shaped microsphere structure covers almost the entire FTO surface, constructing a very uniform electrode of  $\text{Bi}_2\text{WO}_6$ . The high-resolution image of each sphere (Figure 2b) revealed that  $\text{Bi}_2\text{WO}_6$  have superstructures with a buckyball-shaped appearance. These microspheres were in the size range of 0.4 to 0.8  $\mu\text{m}$ . It was understood that the superstructures are mainly composed of 2D nanoparticles with a width around 10–30 nm, as revealed by the SEM. The surfaces of the microspheres were coarse and had many individual nanoparticles. The SEM images also reveal that these nanoparticles were aligned perpendicular to the sphere, pointed to the shared core within the buckyball-shaped microstructure (Figure 2b). More importantly, the microspheres have numerous pores possessing diverse diameters, indicating the potential to provide improved physicochemical characters. Within the microspheres one can easily see some nanoplates formed on the surface of the FTO (Figure 2a,b), which suggests a two-stage growth process of the  $\text{Bi}_2\text{WO}_6$  microspheres. The primary stage is the formation of nanospheres/nanoplates and then these nanoplates self-assembled to form microsphere structures, which is a common phenomenon in the formation of microspheres in the hydrothermal process [5,33]. A cross-section of the electrode (Figure 2c,d) showed the growth of the  $\text{Bi}_2\text{WO}_6$  hierarchical structures on top of each other, increasing the thickness of

the electrode up to 3  $\mu\text{m}$ . The cross-section image further confirmed that each microsphere is about 0.4–0.8  $\mu\text{m}$  in diameter.

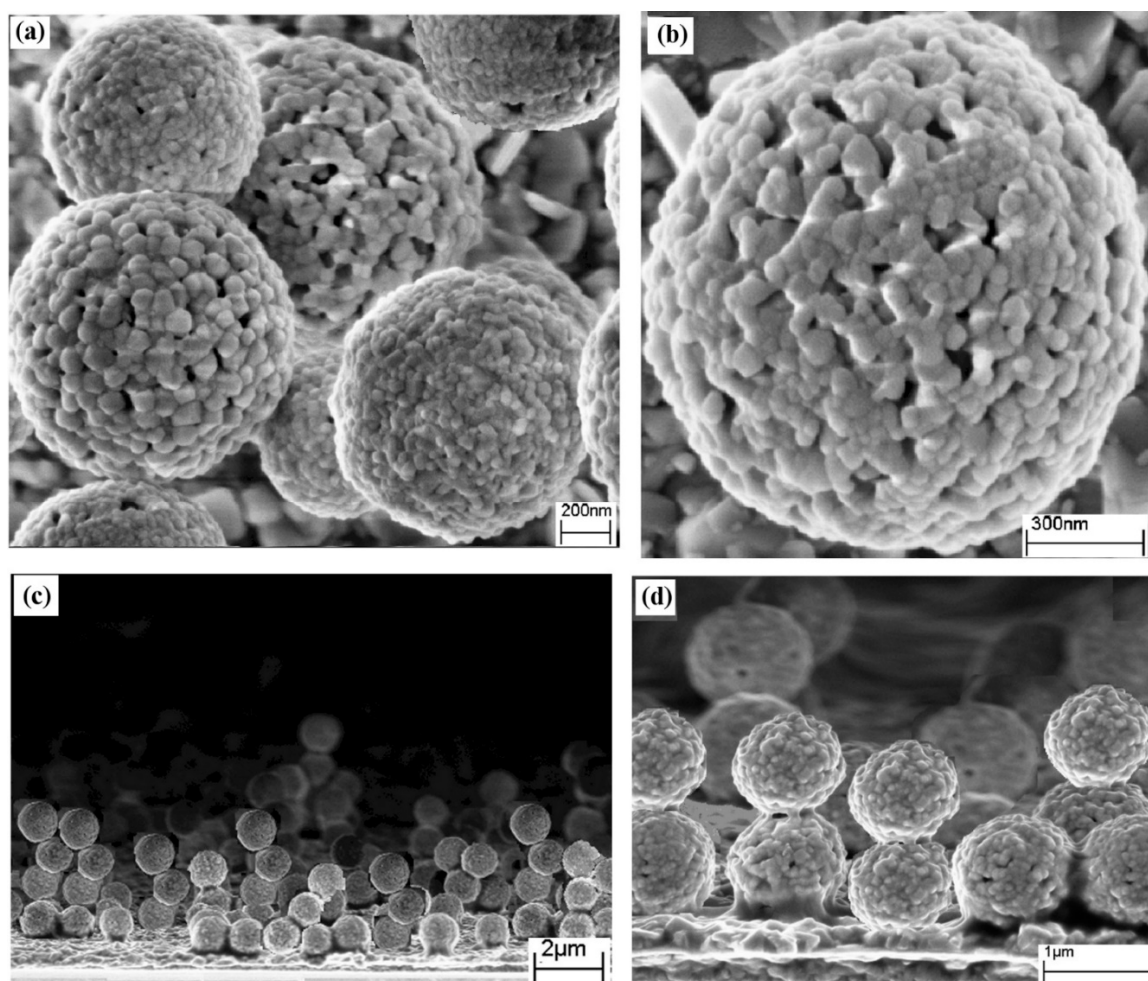


**Figure 2.** The SEM micrographs of hierarchical buckyball-shaped microsphere structured electrodes deposited by Aerosol-Assisted Chemical Vapor Deposition (AACVD) at 500  $^{\circ}\text{C}$ : (a,b) surface morphology, (c,d) cross section of electrodes.

The formation of nanoplates and microsphere structured-based electrodes was also evident from the analysis of XRD data. The intensity ratio of (113) peak to the (200) peak  $I_{(113)}/I_{(200)}$  for the films deposited at 475  $^{\circ}\text{C}$  and 500  $^{\circ}\text{C}$  is 3.6 and 2.8, respectively, which are much smaller than the standard ratio value of five (ICDD 01-073-2020). This relatively low  $I_{(113)}/I_{(200)}$  ratio indicates specific anisotropic growth of crystals along the plane (001). Further analysis shows that at low temperatures (i.e., 400  $^{\circ}\text{C}$ ) the value of the intensity ratio of (113) peak to the (200) peak was near to the standard ratio of 5 and steadily declined with increasing temperature. These changes imply the anisotropic nature of the electrodes. This can be ascribed to their surface structures, which were further confirmed by SEM and agree well with the reported ratio of  $I_{(113)}/I_{(200)}$  for the square plates like morphologies of  $\text{Bi}_2\text{WO}_6$  [10].

#### 3.4. Mechanism of Formation of Nanoplates and Growth of Hierarchical Superstructures by AACVD

The formation of  $\text{Bi}_2\text{WO}_6$  nanoplates and hierarchical microsphere structures by the hydrothermal process has been already explained based on the controlled concentration of  $\text{Bi}^{3+}$  ions by using organic chelating ligands or by increasing the pH of the solution [5,36]. Similarly, in our work, acetate and DAMP play a multifold role in the growth of  $\text{Bi}_2\text{WO}_6$  nanoplates and hierarchical buckyball-shaped microsphere structures. Acetate acted as complexing agents in the precursor solution as it influenced

nucleation and growth rate of  $\text{Bi}_2\text{WO}_6$ . For example, the carboxylate groups of acetate complex with bismuth ions decrease the free ion concentration in the solution. During the deposition process, aerosol droplets travel through different temperature zones; the first step is the evaporation of solvents and the second step is vaporization of the precursor. Therefore, when the acetate complex chelation becomes weak, the release of ions will take place. At a temperature of  $450\text{ }^\circ\text{C}$ , the released ions will be deposited on the substrate surface and subsequently, the nucleation starts. So, the nucleation and growth of particles will undergo a lengthy procedure and consequently results in uniform crystals. The carboxylate groups released are then adsorbed on the surfaces of the newly produced nanocrystals and facilitate the self-assembly to form nanoplates (scheme A in Figure 3).

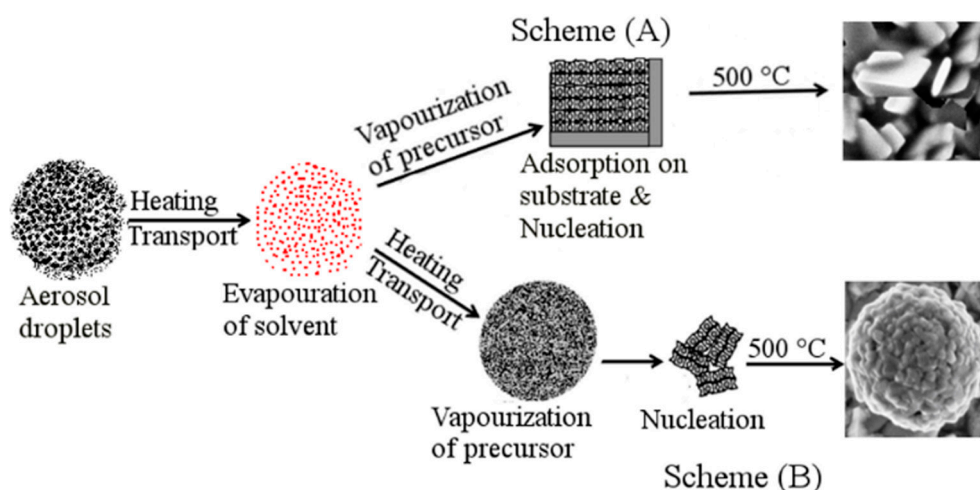


**Figure 3.** A diagrammatic representation of probable development process of nanoplate and hierarchical buckyball-shaped microsphere structures formation during AACVD process.

On the other hand, the formation of hierarchical microsphere structures at an AACVD deposition temperature of  $500\text{ }^\circ\text{C}$ , using a precursor solution, might be defined as a homogeneous decomposition reaction. At a relatively high deposition temperature (i.e.,  $500\text{ }^\circ\text{C}$ ), the main decomposition process takes place during the vapor phase, therefore resulting in homogeneous nucleation which produces fine particles. These fine particles aggregate to form nanoparticles before they are adsorbed onto the substrate. The continuous flow of gases may help these nanoparticles to spin along the *c*-axis to build hierarchical microsphere structures (scheme B in Figure 3). The formation of hierarchical microsphere structures over the top of each other (Figure 2d) is clear evidence for the nucleation and formation of nanoparticles in the vapor phase before they plunge on to the substrate. The deposition process in AACVD is much more complex than the traditional CVD method [37]. Nevertheless, to date there is no specific model to portray the AACVD-procedures fully [38]. It has been hypothesized that the surfaces of nanobuilding blocks modified by organic surface groups form specific aggregation, whereas loosely arranged nanoparticles repeatedly lead to unsystematic aggregation [39]. The control experiments conducted using  $\text{Bi}(\text{NO}_3)_3 \cdot 5\text{H}_2\text{O}$  and  $(\text{NH}_4)_6\text{H}_2\text{W}_{12}\text{O}_{40} \cdot \text{XH}_2\text{O}$  solution in distilled water showed that the particles formed are irregular and dispersed randomly without dimethylaminopropanol (DMAP) ligands (Figure S2 in supporting information).

### 3.5. Optical Characterization

The  $\text{Bi}_2\text{WO}_6$  thin films possess sharp absorption peaks in the visible region [40]. The UV-visible spectra of  $\text{Bi}_2\text{WO}_6$  electrodes have been taken by UV/Vis spectrophotometer. Figure 4 shows the bandgap of  $\text{Bi}_2\text{WO}_6$  film electrodes, (a) for hierarchical buckyball-shaped microsphere structured electrodes deposited by AACVD at  $500\text{ }^\circ\text{C}$  and (b) for nanoplate-like electrodes deposited by AACVD at  $500\text{ }^\circ\text{C}$ . The bandgap ( $E_g$ ) of the electrodes was calculated using the Tauc plot equation  $(ah\nu)^n =$

$A(h\nu - E_g)$  and were found to be 2.81 and 2.85 eV, respectively. The results obtained are similar to those previously reported for  $\text{Bi}_2\text{WO}_6$  powder nanoparticles [5].

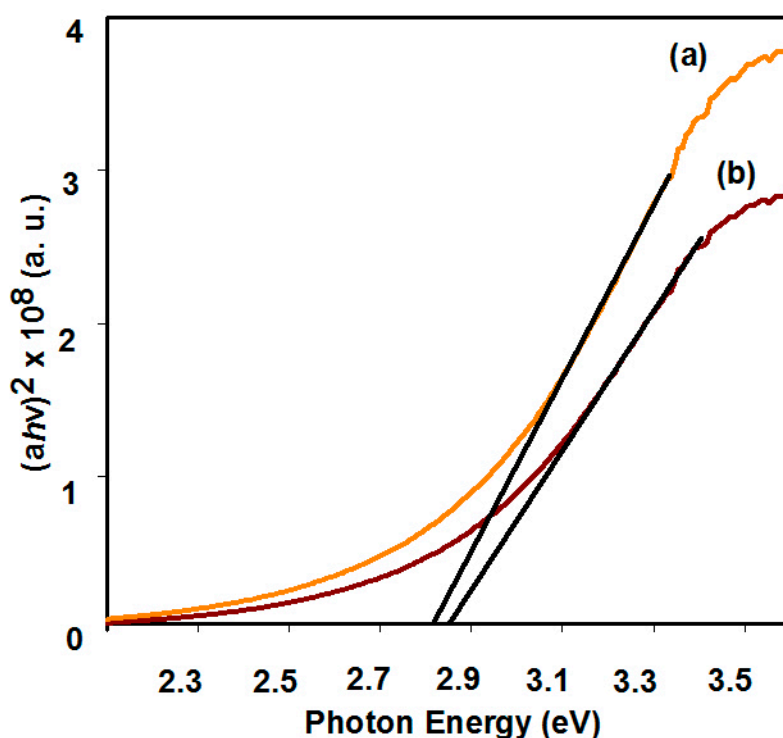


**Figure 4.** Plot of  $(ah\nu)^2$  versus photon energy  $(h\nu)$  for  $\text{Bi}_2\text{WO}_6$  electrodes deposited by AACVD deposited at 500 °C, (a) hierarchical buckyball-like microsphere and (b) nanoplates.

### 3.6. Photoelectrochemical Characterisation

The PEC measurements of the  $\text{Bi}_2\text{WO}_6$  electrodes were studied by way of the 3-electrode approach, using AM 1.5 illumination. The current density plots in Figure 5 revealed the relation between photocurrent density and deposition temperature. The  $J$ - $V$  curves in Figure 5 illustrate the change of photocurrent onset in the direction of negative potentials for hierarchical buckyball-shaped microsphere electrodes deposited by AACVD. The negative shift of the photocurrent may be as a result of (001) preferred plane orientation of the grain particles and electrodes' surface structure. Hence, the data obtained confirm that there is a direct relationship between photocurrent and the deposition temperature. The grain size, orientation and surface structure of the electrodes changed significantly with the deposition temperature. For all electrodes, increase in deposition temperature improved the photocurrent density. Additional amplification of deposition temperature could not carry on after a definite point owing to the volatility of the glass substrate at an elevated temperature ( $>500$  °C), premature decomposition of aerosol and film adherence issues experienced at high temperatures. Therefore, the surface structure and specific orientation are the vital parameters for estimating the wavelength and charge transfer properties [41].

Figure 6 demonstrates the photocurrent measurements under chopping light at regular intervals to reveal light and dark current simultaneously. The steady-state  $J$ - $V$  plot was overlaid on the chopped plot in each case to compare steady-state and transient photocurrent and both show good agreement. By far the best  $\text{Bi}_2\text{WO}_6$  photoelectrode is that with hierarchical buckyball-shaped microsphere morphology. We attribute this to the hierarchical microsphere structures and (001) preferred orientation plane. The negative shift of the photocurrent onset related to preferred orientation along (001) plane provides a route to engineering the energetic and interfacial charge transfer properties at  $\text{Bi}_2\text{WO}_6$  electrode/electrolyte interface. Along with the preferred crystallographic orientation, the hierarchical microsphere structures have numerous microspores and a high internal surface area that



permits more electrolytes in the form of electrolytic solution to enter all microspheres giving a big semiconductor/electrolyte interface. The  $220 \mu\text{Acm}^{-2}$  photocurrent density at 0.23 V (vs. Ag/AgCl/3M KCl) under AM1.5 illumination, as well as a negligible dark current (Figure 6) for hierarchical buckyball-shaped microsphere electrodes. is among the highest photocurrent density for  $\text{Bi}_2\text{WO}_6$  electrodes reported to date. It was revealed that the light absorption properties of  $\text{Bi}_2\text{WO}_6$  electrodes influenced by the preparation method will affect the surface structure and specific orientation of the electrodes [42].

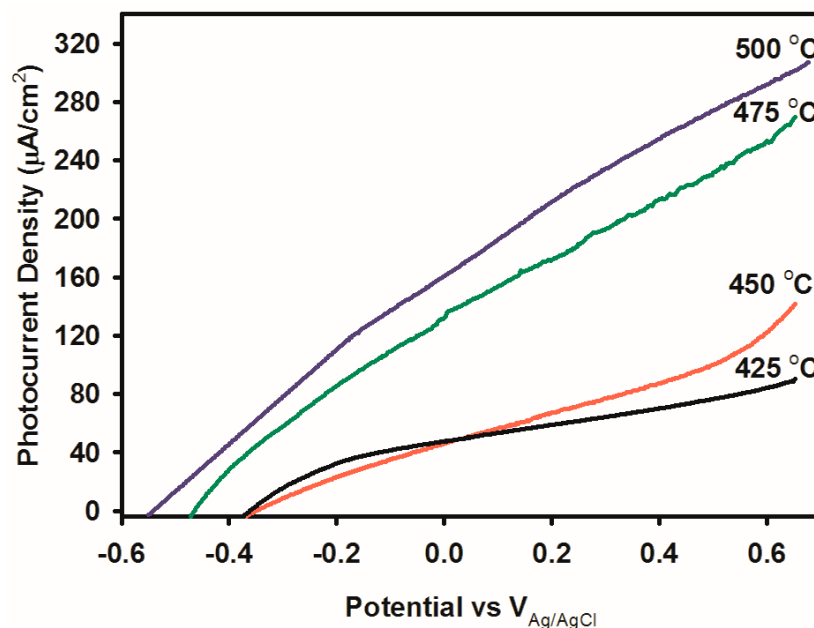


**Figure 5.** Photocurrent-voltage plots showing the deposition temperature dependence of photocurrent of  $\text{Bi}_2\text{WO}_6$  electrodes deposited by AACVD.

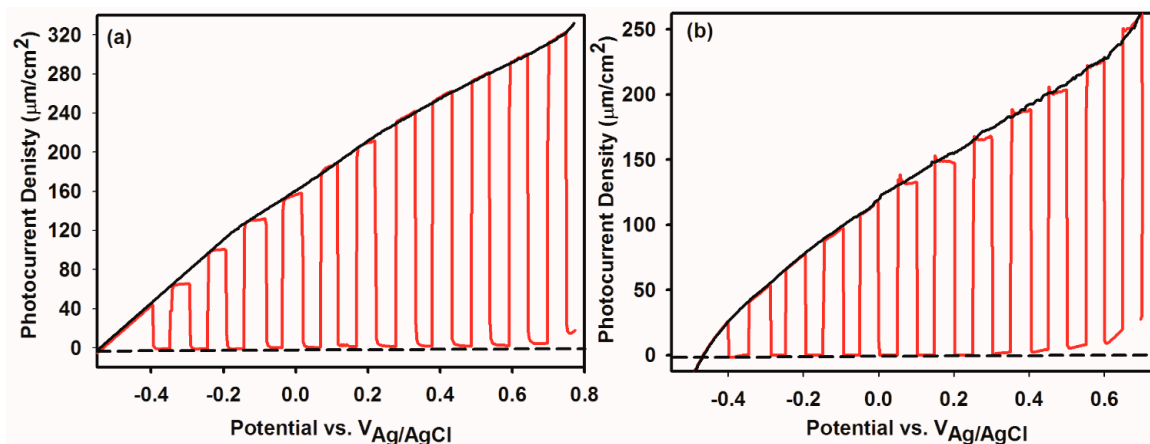


**Figure 6.** Current-voltage characteristics (a) for Hierarchical buckyball-shaped microsphere structured and (b) for nanoplates structured for  $\text{Bi}_2\text{WO}_6$  electrodes deposited by AACVD. The light was physically chopped to reveal light and dark current concurrently.

### 3.7. Photocatalytic dye Degradation Studies

The photocatalytic activity of  $\text{Bi}_2\text{WO}_6$  photoelectrodes was investigated for the decomposition of methylene blue (MB) and rhodamine B (RhB), in visible light illumination. Figure 7 shows the absorbance of MB and RhB dyes at different intervals during the photocatalytic reaction. Electrodes with a hierarchical buckyball-shaped microsphere structure exhibit higher photocatalytic activity than electrodes with nanoplates structures. The  $\text{Bi}_2\text{WO}_6$  photoelectrodes show a much higher photocatalytic

efficiency for RhB dye compared to MB. After 30 min of visible light illumination, the RhB removal over  $\text{Bi}_2\text{WO}_6$  photoelectrodes with a hierarchical buckyball-shaped microsphere structure arrives at 99%, obviously higher than the value of 65% for the MB dye. Meanwhile,  $\text{Bi}_2\text{WO}_6$  photoelectrodes with nanoplates structures show photocatalytic efficiency of 90% and 60% for RhB and MB respectively, after the same duration of light illumination.

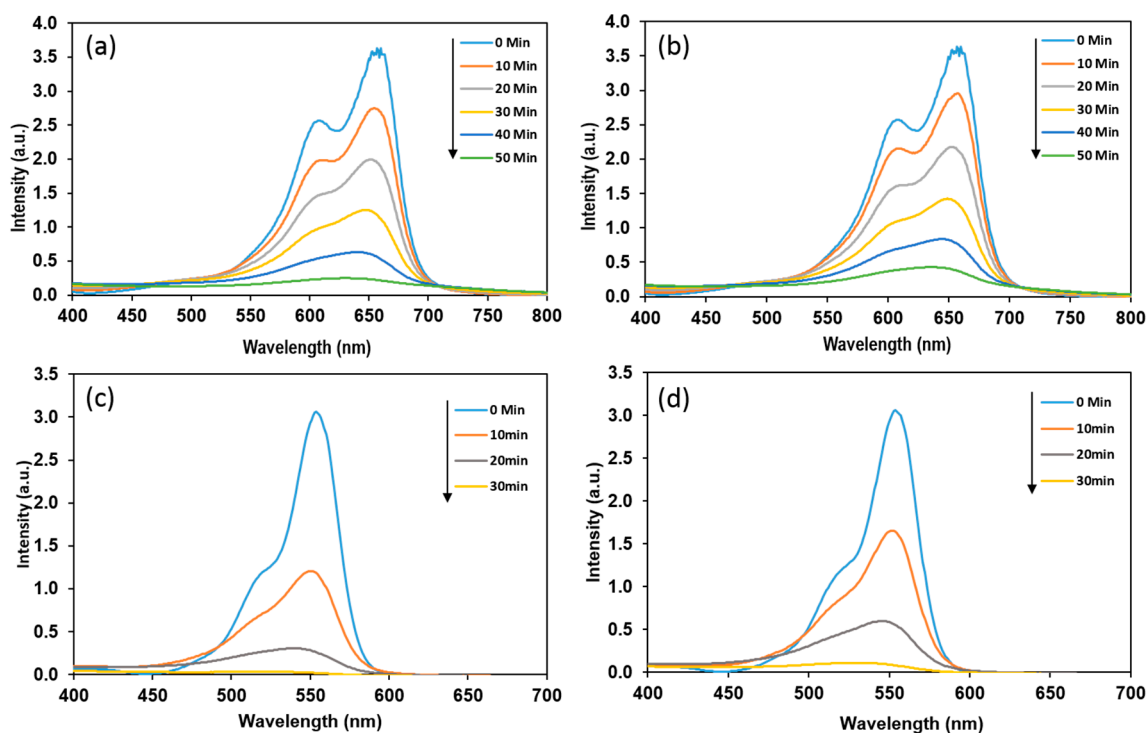


**Figure 7.** Photocatalytic degradation activity of  $\text{Bi}_2\text{WO}_6$  prepared at different flow rates, (a) methylene blue using  $\text{Bi}_2\text{WO}_6$  nanoplates electrodes (MB-P), (b) methylene blue using  $\text{Bi}_2\text{WO}_6$  hierarchical buckyball-shaped microsphere electrodes (MB-B), (c) rhodamine B using  $\text{Bi}_2\text{WO}_6$  hierarchical buckyball-shaped microsphere electrodes (RhB-B), (d) rhodamine B using  $\text{Bi}_2\text{WO}_6$  nanoplates electrodes (RhB-P).

The photocatalytic efficiency of  $\text{Bi}_2\text{WO}_6$  photoelectrodes in the photochemical decomposition of MB and RhB was determined using the following expression:

$$\% \text{ Degradation} = \frac{C_0 - C}{C_0} \times 100 \quad (1)$$

where  $C_0$  is the initial concentration of dye in mg/L and  $C$  is the remaining concentration of dye after illumination in time interval. The efficiency of the photocatalysis of  $\text{Bi}_2\text{WO}_6$  photoelectrodes was estimated by photodegradation of MB and RhB as a function of  $C_0/C$  versus duration of irradiation as shown in Figure 8.

The initial decomposition reaction was calculated using pseudo-first-order kinetic law.

$$-\text{Ln} \frac{C}{C_0} = k_{app} t \quad (2)$$

where  $k_{app}$  is the pseudo-first-order rate constant and  $t$  is the time of reaction. In order to confirm the estimation,  $\text{Ln}(C/C_0)$  versus illumination time yields a straight line with a slope of  $k_{app}$  as shown in Figure 9. Because the straight lines were obtained as expected, the kinetics of RhB photo-degradation described the first-order degradation curve, which coincides with the L-H model [43].

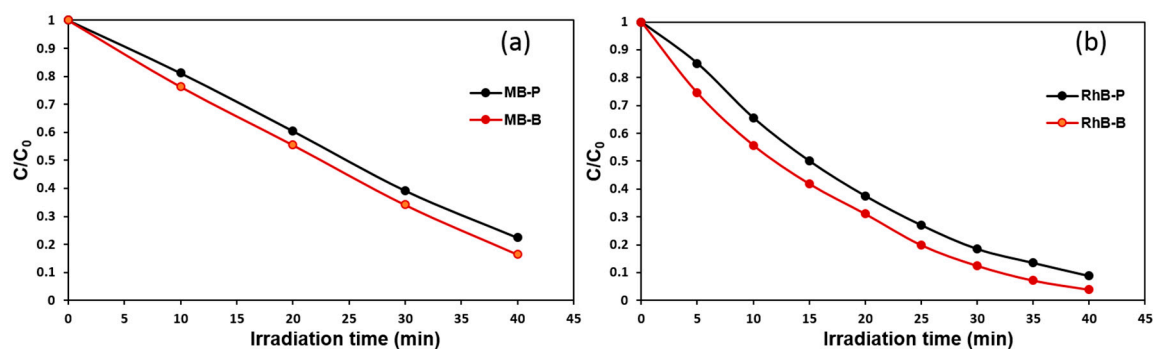


**Figure 8.** The plot of  $C/C_0$  vs. time of irradiation for  $\text{Bi}_2\text{WO}_6$  films (a) for MB dye and (b) for RhB dye.

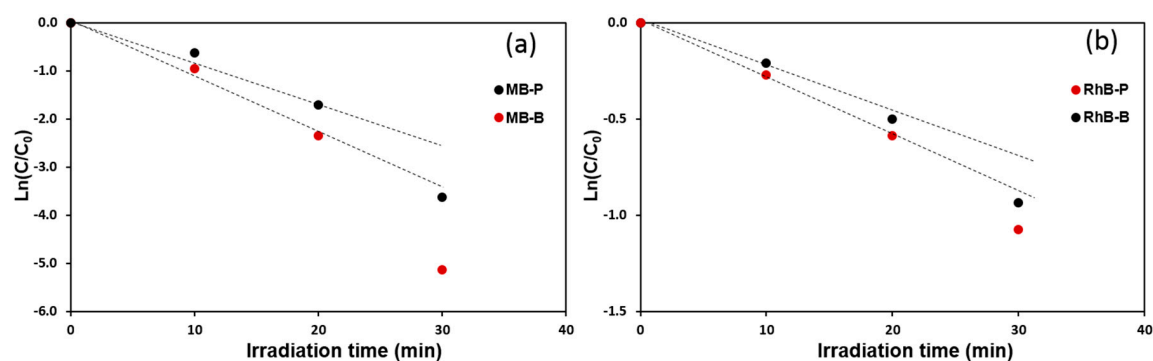


**Figure 9.** Kinetic plot of  $\text{Ln}(C/C_0)$  vs. time of irradiation for photocatalytic degradation of (a) MB dye and (b) with RhB dye.

The reaction rate constants ( $k_{app}$ ) observed for photodegradation are pseudo-first-order kinetics and the half-life parameters are presented in Table 1. The data present in the Table 1 approve the observation described previously, where the decrease in the flow rate leads to the formation of a hierarchical buckyball-shaped microsphere structured electrode, which exhibits a photocatalytic activity higher than a nanoplates structured electrode. The observed increase in rate constants of  $\text{Bi}_2\text{WO}_6$  electrodes with a hierarchical buckyball-shaped microsphere structure could be attributed to their morphological and crystalline properties [44]. SEM of  $\text{Bi}_2\text{WO}_6$  electrodes with a hierarchical buckyball-shaped microsphere structure presents greater crystallinity and particle size in comparison with the nanoplates structured electrode, and considering that the higher crystallinity of a material shows lower defects on its surface, which generally act as electron-hole recombination centres; thus, materials with high crystallinity possess high photocatalytic activity [45,46]. In Table 1, it can be observed that the removal rate of RhB dye was better than that of MB dye. After 30 min of exposure to visible light, the RhB removal over  $\text{Bi}_2\text{WO}_6$  electrodes with a hierarchical buckyball-shaped microsphere structure was 99%, obviously higher than the value of 65% for MB, as shown in Figure 7. This could be attributed to the variation in dye chemical structure, which leads to variance in adsorption properties and in capability to degradation [47].

**Table 1.** Pseudo-first order rate constants and half-life for the degradation of MB and RhB dyes.

Catalysts	$k_{app}(\text{min}^{-1})$		$t_{1/2}(\text{min})$	
	MB	RhB	MB	RhB
$\text{Bi}_2\text{WO}_6\text{-B}$	0.054	0.157	20	7
$\text{Bi}_2\text{WO}_6\text{-P}$	0.044	0.116	23	12

#### 4. Conclusions

We have demonstrated, for the first time, a simple method for the preparation of Bi<sub>2</sub>WO<sub>6</sub> electrodes with nanoplates and hierarchical buckyball-shaped microsphere structured morphologies by appropriately controlling the parameters of the AACVD process. The fabrication method, precursor solution, deposition temperature and carrier gas flow have a big impact on the surface structure and orientation of Bi<sub>2</sub>WO<sub>6</sub> electrodes. Electrodes can be reproduced easily and show a bandgap energy of ~2.8 eV and display anodic photocurrent. Bi<sub>2</sub>WO<sub>6</sub> electrodes with a hierarchical buckyball-shaped microsphere structure have shown a photocurrent density of 220  $\mu\text{Acm}^{-2}$  while nanoplates had 170  $\mu\text{Acm}^{-2}$  photocurrent density at 0.23 V (vs. Ag/AgCl/3M KCl) in AM1.5 illumination. Similarly, Bi<sub>2</sub>WO<sub>6</sub> electrodes with a hierarchical buckyball-shaped microsphere structure have 99% RhB and 65% of MB photocatalytic degradation in 30 min while nanoplates showed photocatalytic efficiency of 90% and 60% for RhB and MB, respectively.

In this work, we have shown that PEC and photocatalytic properties of Bi<sub>2</sub>WO<sub>6</sub> electrodes can be significantly enhanced by the systematic control of morphology and orientation. We assume that this study will initiate the utilization of Bi<sub>2</sub>WO<sub>6</sub> electrodes in diverse fields like photodegradation, electronic and electrochemical applications.

**Supplementary Materials:** The following are available online at <http://www.mdpi.com/2079-4991/9/5/755/s1>, Figure S1: Raman Spectra of Bi<sub>2</sub>WO<sub>6</sub> electrodes, Figure S2: The SEM micrograph of Bi<sub>2</sub>WO<sub>6</sub> electrode deposited by AACVD using Bi(NO<sub>3</sub>)<sub>3</sub>·5H<sub>2</sub>O and (NH<sub>4</sub>)<sub>6</sub> H<sub>2</sub>W<sub>12</sub>O<sub>40</sub>·XH<sub>2</sub>O solution in distilled water without dimethylaminopropanol (DMAP) deposited at 500 °C.

**Author Contributions:** Conceptualization, A.A.T. and H.B.; methodology, B.Y.A. and A.A.T.; formal analysis, B.Y.A. and H.B.; data curation, B.A.Y.; supervision, A.A.T. Writing-Original Draft Preparation, A.A.T. and H.B.; Writing-Review & Editing, A.A.T. and H.B.

**Acknowledgments:** The financial support was provided by Engineering and Physical Science Research Council, UK (EPSRC) under the research grant No EP/P510956/1 and EP/R512801/1. We also acknowledge UKIERI-DST2016-17-0089 project for partly funding the present work. NSG Pilkington Glass Ltd. is acknowledged for kindly providing the FTO substrates for this work.

**Conflicts of Interest:** The authors declare no conflict of interest.

#### References

1. Niu, K.; Yang, J.; Kulinich, S.; Sun, J.; Li, H.; Du, X. Morphology control of nanostructures via surface reaction of metal nanodroplets. *J. Am. Chem. Soc.* **2010**, *132*, 9814–9819. [[CrossRef](#)]
2. Amano, F.; Nogami, K.; Ohtani, B. Visible light-responsive bismuth tungstate photocatalysts: Effects of hierarchical architecture on photocatalytic activity. *J. Phys. Chem. C* **2009**, *113*, 1536–1542. [[CrossRef](#)]
3. Buonsanti, R.; Grillo, V.; Carlino, E.; Giannini, C.; Gozzo, F.; Garcia-Hernandez, M.; Garcia, M.A.; Cingolani, R.; Cozzoli, P.D. Architectural Control of Seeded-Grown Magnetic–Semiconductor Iron Oxide–TiO<sub>2</sub> Nanorod Heterostructures: The Role of Seeds in Topology Selection. *J. Am. Chem. Soc.* **2010**, *132*, 2437–2464. [[CrossRef](#)]
4. Whang, D.; Jin, S.; Wu, Y.; Lieber, C.M. Large-scale hierarchical organization of nanowire arrays for integrated nanosystems. *Nano Lett.* **2003**, *3*, 1255–1259. [[CrossRef](#)]
5. Zhang, L.; Wang, W.; Zhou, L.; Xu, H. Bi<sub>2</sub>WO<sub>6</sub> Nano- and Microstructures: Shape Control and Associated Visible-Light-Driven Photocatalytic Activities. *Small* **2007**, *3*, 1618–1625. [[CrossRef](#)]
6. Kuang, D.; Brezesinski, T.; Smarsly, B. Hierarchical porous silica materials with a trimodal pore system using surfactant templates. *J. Am. Chem. Soc.* **2004**, *126*, 10534–10535. [[CrossRef](#)] [[PubMed](#)]
7. Wang, Y.; Zhu, Q.; Zhang, H. Fabrication and magnetic properties of hierarchical porous hollow nickel microspheres. *J. Mater. Chem.* **2006**, *16*, 1212–1214. [[CrossRef](#)]
8. Tian, Y.; Chang, B.; Lu, J.; Fu, J.; Xi, F.; Dong, X. Hydrothermal Synthesis of Graphitic Carbon Nitride–Bi<sub>2</sub>WO<sub>6</sub> Heterojunctions with Enhanced Visible Light Photocatalytic Activities. *ACS Appl. Mater. Interfaces* **2013**, *5*, 7079–7085. [[CrossRef](#)]
9. Chen, S.; Fan, Z.; Carroll, D.L. Silver nanodisks: Synthesis, characterization and self-assembly. *J. Phys. Chem. B* **2002**, *106*, 10777–10781. [[CrossRef](#)]

10. Li, Y.; Liu, J.; Huang, X.; Li, G. Hydrothermal synthesis of Bi<sub>2</sub>WO<sub>6</sub> uniform hierarchical microspheres. *Cryst. Growth Des.* **2007**, *7*, 1350–1355. [[CrossRef](#)]
11. Liang, C.; Shimizu, Y.; Sasaki, T.; Umehara, H.; Koshizaki, N. Au-mediated growth of wurtzite ZnS nanobelts, nanosheets and nanorods via thermal evaporation. *J. Phys. Chem. B* **2004**, *108*, 9728–9733. [[CrossRef](#)]
12. Gautam, U.K.; Vivekchand, S.; Govindaraj, A.; Kulkarni, G.; Selvi, N.; Rao, C. Generation of onions and nanotubes of GaS and GaSe through laser and thermally induced exfoliation. *J. Am. Chem. Soc.* **2005**, *127*, 3658–3659. [[CrossRef](#)]
13. Wakiya, N.; Muraoka, K.; Kadowaki, T.; Kiguchi, T.; Mizutani, N.; Suzuki, H.; Shinozaki, K. Preparation of ferromagnetic zinc-ferrite thin film by pulsed laser deposition in the magnetic field. *J. Magn. Magn. Mater.* **2007**, *310*, 2546–2548. [[CrossRef](#)]
14. Kobayashi, M.; Shirai, H.; Nunokawa, M. High-temperature sulfidation behavior of reduced zinc ferrite in simulated coal gas revealed by in situ X-ray diffraction analysis and Mössbauer spectroscopy. *Energy Fuels* **2002**, *16*, 601–607. [[CrossRef](#)]
15. Abe, M.; Itoh, T.; Tamaura, Y.; Gomi, M. Ferrite-organic multilayer film for microwave monolithic integrate circuits prepared by ferrite plating based on the spray-spin-coating method. *J. Appl. Phys.* **1988**, *63*, 3774–3776. [[CrossRef](#)]
16. Huang, Y.; Ai, Z.; Ho, W.; Chen, M.; Lee, S. Ultrasonic spray pyrolysis synthesis of porous Bi<sub>2</sub>WO<sub>6</sub> microspheres and their visible-light-induced photocatalytic removal of NO. *J. Phys. Chem. C* **2010**, *114*, 6342–6349. [[CrossRef](#)]
17. Zhang, R.; Huang, J.; Zhao, J.; Sun, Z.; Wang, Y. Sol-gel auto-combustion synthesis of zinc ferrite for moderate temperature desulfurization. *Energy Fuels* **2007**, *21*, 2682–2687. [[CrossRef](#)]
18. Atif, M.; Hasanain, S.; Nadeem, M. Magnetization of sol-gel prepared zinc ferrite nanoparticles: Effects of inversion and particle size. *Solid State Commun.* **2006**, *138*, 416–421. [[CrossRef](#)]
19. Ishikawa, K.; Watanabe, T.; Funakubo, H. Preparation of Bi<sub>2</sub>WO<sub>6</sub> thin films by metalorganic chemical vapor deposition and their electrical properties. *Thin Solid Films* **2001**, *392*, 128–133. [[CrossRef](#)]
20. Zhao, X.; Wu, Y.; Yao, W.; Zhu, Y. Photoelectrochemical properties of thin Bi<sub>2</sub>WO<sub>6</sub> films. *Thin Solid Films* **2007**, *515*, 4753–4757. [[CrossRef](#)]
21. Li, J.; Zhang, X.; Ai, Z.; Jia, F.; Zhang, L.; Lin, J. Efficient visible light degradation of rhodamine B by a photo-electrochemical process based on a Bi<sub>2</sub>WO<sub>6</sub> nanoplate film electrode. *J. Phys. Chem. C* **2007**, *111*, 6832–6836. [[CrossRef](#)]
22. Mann, A.K.; Skrabalak, S.E. Synthesis of single-crystalline nanoplates by spray pyrolysis: A metathesis route to Bi<sub>2</sub>WO<sub>6</sub>. *Chem. Mater.* **2011**, *23*, 1017–1022. [[CrossRef](#)]
23. Zhang, S.; Shen, J.; Fu, H.; Dong, W.; Zheng, Z.; Shi, L. Bi<sub>2</sub>WO<sub>6</sub> photocatalytic films fabricated by layer-by-layer technique from Bi<sub>2</sub>WO<sub>6</sub> nanoplates and its spectral selectivity. *J. Solid State Chem.* **2007**, *180*, 1456–1463. [[CrossRef](#)]
24. He, D.; Wang, L.; Xu, D.; Zhai, J.; Wang, D.; Xie, T. Investigation of photocatalytic activities over Bi<sub>2</sub>WO<sub>6</sub>/ZnWO<sub>4</sub> composite under UV light and its photoinduced charge transfer properties. *ACS Appl. Mater. Interfaces* **2011**, *3*, 3167–3171. [[CrossRef](#)] [[PubMed](#)]
25. Zhang, C.; Zhu, Y. Synthesis of square Bi<sub>2</sub>WO<sub>6</sub> nanoplates as high-activity visible-light-driven photocatalysts. *Chem. Mater.* **2005**, *17*, 3537–3545. [[CrossRef](#)]
26. Saison, T.; Gras, P.; Chemin, N.; Chanéac, C.; Durupthy, O.; Brezova, V.; Colbeau-Justin, C.; Jolivet, J.-P. New Insights into Bi<sub>2</sub>WO<sub>6</sub> Properties as a Visible-Light Photocatalyst. *J. Phys. Chem. C* **2013**, *117*, 22656–22666. [[CrossRef](#)]
27. Yan, Y.; Wu, Y.; Yan, Y.; Guan, W.; Shi, W. Inorganic-Salt-Assisted Morphological Evolution and Visible-Light-Driven Photocatalytic Performance of Bi<sub>2</sub>WO<sub>6</sub> Nanostructures. *J. Phys. Chem. C* **2013**, *117*, 20017–20028. [[CrossRef](#)]
28. Osterloh, F.E. Inorganic materials as catalysts for photochemical splitting of water. *Chem. Mater.* **2007**, *20*, 35–54. [[CrossRef](#)]
29. Shang, M.; Wang, W.; Ren, J.; Sun, S.; Wang, L.; Zhang, L. A practical visible-light-driven Bi<sub>2</sub>WO<sub>6</sub> nanofibrous mat prepared by electrospinning. *J. Mater. Chem.* **2009**, *19*, 6213–6218. [[CrossRef](#)]
30. Zhou, Y.; Tian, Z.; Zhao, Z.; Liu, Q.; Kou, J.; Chen, X.; Gao, J.; Yan, S.; Zou, Z. High-yield synthesis of ultrathin and uniform Bi<sub>2</sub>WO<sub>6</sub> square nanoplates benefitting from photocatalytic reduction of CO<sub>2</sub> into renewable hydrocarbon fuel under visible light. *ACS Appl. Mater. Interfaces* **2011**, *3*, 3594–3601. [[CrossRef](#)]

31. Alfaifi, B.Y.; Ullah, H.; Alfaifi, S.; Tahir, A.A.; Mallick, T.K. Photoelectrochemical solar water splitting: From basic principles to advanced devices. *Veruscript Funct. Nanomater.* **2018**, *2*, 1–26. [[CrossRef](#)]
32. Tahir, A.A.; Wijayantha, K.U.; Saremi-Yarahmadi, S.; Mazhar, M.; McKee, V. Nanostructured  $\alpha$ -Fe<sub>2</sub>O<sub>3</sub> thin films for photoelectrochemical hydrogen generation. *Chem. Mater.* **2009**, *21*, 3763–3772. [[CrossRef](#)]
33. Ma, D.; Huang, S.; Chen, W.; Hu, S.; Shi, F.; Fan, K. Self-assembled three-dimensional hierarchical umbilicate Bi<sub>2</sub>WO<sub>6</sub> microspheres from nanoplates: Controlled synthesis, photocatalytic activities and wettability. *J. Phys. Chem. C* **2009**, *113*, 4369–4374. [[CrossRef](#)]
34. Crane, M.; Frost, R.L.; Williams, P.A.; Kloprogge, J.T. Raman spectroscopy of the molybdate minerals chillagite (tungsteinian wulfenite-I4), stolzite, scheelite, wolframite and wulfenite. *J. Raman Spectrosc.* **2002**, *33*, 62–66. [[CrossRef](#)]
35. Maczka, M.; Macalik, L.; Hermanowicz, K.; Kępiński, L.; Tomaszewski, P. Phonon properties of nanosized bismuth layered ferroelectric material—Bi<sub>2</sub>WO<sub>6</sub>. *J. Raman Spectrosc.* **2010**, *41*, 1059–1066. [[CrossRef](#)]
36. Wu, J.; Duan, F.; Zheng, Y.; Xie, Y. Synthesis of Bi<sub>2</sub>WO<sub>6</sub> nanoplate-built hierarchical nest-like structures with visible-light-induced photocatalytic activity. *J. Phys. Chem. C* **2007**, *111*, 12866–12871. [[CrossRef](#)]
37. Pierson, H.O. *Handbook of Chemical Vapor Deposition: Principles, Technology and Applications*; William Andrew: Washington, DC, USA, 1999.
38. Hou, X.; Choy, K.L. Processing and Applications of Aerosol-Assisted Chemical Vapor Deposition. *Chem. Vap. Depos.* **2006**, *12*, 583–596. [[CrossRef](#)]
39. Zhang, Z.; Sun, H.; Shao, X.; Li, D.; Yu, H.; Han, M. Three-Dimensionally Oriented Aggregation of a Few Hundred Nanoparticles into Monocrystalline Architectures. *Adv. Mater.* **2005**, *17*, 42–47. [[CrossRef](#)]
40. Kudo, A.; Tsuji, I.; Kato, H. AgInZn 7 S 9 solid solution photocatalyst for H<sub>2</sub> evolution from aqueous solutions under visible light irradiation. *Chem. Commun.* **2002**, *17*, 1958–1959. [[CrossRef](#)]
41. Yang, B.; Zhang, Y.; Drabarek, E.; Barnes, P.R.; Luca, V. Enhanced photoelectrochemical activity of sol-gel tungsten trioxide films through textural control. *Chem. Mater.* **2007**, *19*, 5664–5672. [[CrossRef](#)]
42. Zhang, L.W.; Wang, Y.J.; Cheng, H.Y.; Yao, W.Q.; Zhu, Y.F. Synthesis of Porous Bi<sub>2</sub>WO<sub>6</sub> Thin Films as Efficient Visible-Light-Active Photocatalysts. *Adv. Mater.* **2009**, *21*, 1286–1290. [[CrossRef](#)]
43. Chen, H.; Zahraa, O.; Bouchy, M.; Thomas, F.; Bottero, J. Adsorption properties of TiO<sub>2</sub> related to the photocatalytic degradation of organic contaminants in water. *J. Photochem. Photobiol. A Chem.* **1995**, *85*, 179–186. [[CrossRef](#)]
44. Huang, C.; Zhu, K.; Qi, M.; Zhuang, Y.; Cheng, C. Preparation and photocatalytic activity of bicrystal phase TiO<sub>2</sub> nanotubes containing TiO<sub>2</sub>-B and anatase. *J. Phys. Chem. Solids* **2012**, *73*, 757–761. [[CrossRef](#)]
45. Alfaifi, B.Y.; Tahir, A.A.; Wijayantha, K.U. Fabrication of Bi<sub>2</sub>WO<sub>6</sub> photoelectrodes with enhanced photoelectrochemical and photocatalytic performance. *Solar Energy Mater. Solar Cells* **2019**, *195*, 134–141. [[CrossRef](#)]
46. Sifontes, A.B.; Roales, M.; Méndez, F.J.; Oviedo, O.; Zoltan, T. Effect of calcination temperature on structural properties and photocatalytic activity of ceria nanoparticles synthesized employing chitosan as template. *J. Nanomater.* **2013**, *2013*, 1. [[CrossRef](#)]
47. Hashemzadeh, F.; Rahimi, R.; Gaffarinejad, A. Photocatalytic degradation of methylene blue and rhodamine B dyes by niobium oxide nanoparticles synthesized via hydrothermal method. *Int. J. Appl. Chem. Sci. Res.* **2013**, *1*, 95–102.

